Article:
Hamling, IJ, Wright, TJ, Calais, E et al. (2014) InSAR observations of post-rifting deformation around the Dabbahu rift segment, Afar, Ethiopia. Geophysical Journal International, 197 (1). 33 - 49. ISSN: 0956-540X

https://doi.org/10.1093/gji/ggu003

Geophysical Journal International

Geophys. J. Int. (2014) **197,** 33–49
Advance Access publication 2014 February 13

doi: 10.1093/gji/ggu003

InSAR observations of post-rifting deformation around the Dabbahu rift segment, Afar, Ethiopia

Ian J. Hamling,[1,2] Tim J. Wright,[2] Eric Calais,[3] Elias Lewi[4] and Yukitoshi Fukahata[5]

[1] *GNS Science, PO Box* 30368, *Avalon, Lower Hutt, New Zealand. E-mail: I.Hamling@gns.cri.nz*
[2] *COMET+ School of Earth and Environment, University of Leeds, Leeds, LS*2 9*JT, UK*
[3] *Department of Earth and Atmospheric Sciences, Purdue University, West Lafayette,* 47907-2051, *Indiana*
[4] *Institute for Geophysics, Space Science and Astronomy, Addis Ababa University, Addis Ababa,* 1176, *Ethiopia*
[5] *Disaster Prevention Research Institute, Kyoto University, Kyoto,* 611-0011, *Japan*

Accepted 2014 January 6. Received 2014 January 5; in original form 2013 July 18

SUMMARY

Increased displacement rates have been observed following manylarge earthquakes and magmatic events. Although an order of magnitude smaller than the displacements associated with the main event, the post-seismic or post-rifting deformation may continue for years to decades after the initial earthquake or dyke intrusion. Due to the rare occurrence of subaerial rifting events, there are very few observations to constrain models of post-rifting deformation. In 2005 September, a 60-km-long dyke was intruded along the Dabbahu segment of the Nubia-Arabia Plate boundary (Afar, Ethiopia), marking the beginning of an ongoing rifting episode. Continued activity has been monitored using satellite radar interferometry and data from global positioning system instruments deployed around the rift in response to the initial intrusion. Using multiple satellite passes, we are able to separate the rift perpendicular and vertical displacement fields around the Dabbahu segment. Rift perpendicular and vertical rates of up to 180 and 240 mm yr^{-1}, respectively. Here, we show that models of viscoelastic relaxation alone are insufficient to reproduce the observed deformation field and that a large portion of the observed signal is related to the movement of magma within the rift segment. Our models suggest upper mantle viscosities of 10^{18-19} Pa s overlain by an elastic crust of between 15 and 30 km. To fit the observations, inflation and deflation of magma chambers in the centre of the rift and to the south east of the rift axis is required at rates of ∼0.13 and −0.08 km^3 yr^{-1}.

Key words: Radar interferometry; Continental margins: divergent; Rheology: crust and lithosphere; Africa.

1 INTRODUCTION

Oceanic lithosphere, which covers over two-thirds of the Earth's surface, is formed at mid-ocean ridges through the upwelling of hot mantle rocks which ascend to fill the gap between separating tectonic plates. Despite the large proportion of the Earth covered by oceanic lithosphere our understanding of the processes involved in oceanic rifting is constrained by a few, albeit well documented, episodes along segments of the Juan de Fuca ridge (e.g. Dziak *et al.* 1995, 2007), East Pacific Rise (e.g. Tolstoy *et al.* 2006; Dziak *et al.* 2009) and Mid-Atlantic Ridge (e.g. Tolstoy *et al.* 2001; Dziak *et al.* 2004). However, subaerial rifting episodes provide the rare opportunity to examine the tectonic and magmatic processes at mid-ocean ridges without the use of submersible instruments Wright *et al.* (2012). The most recent known examples occurred at Krafla in north Iceland (Einarsson & Brandsdóttir 1980; Tryggvason 1984; Buck *et al.* 2006), in the Asal rift (Republic of Djibouti; Abdallah *et al.* 1979; Cattin *et al.* 2005a; Vigny *et al.* 2007) and most recently the Dabbahu rifting episode in central Afar (Ethiopia, Fig. 1; Wright *et al.* 2006; Ayele *et al.* 2009; Hamling *et al.* 2009; Ebinger *et al.* 2010; Grandin *et al.* 2010a,b; Hamling *et al.* 2010).

Increased displacement rates have been observed following many large earthquakes and magmatic events. Although an order of magnitude smaller than the displacements associated with the main event, the post-seismic or post-rifting deformation may continue for years to decades after the initial earthquake or dyke intrusion. Following the Krafla and Asal rifting episodes horizontal displacements were ∼3 times larger than the time-averaged spreading rates between 1987 and 1990 at Krafla and between 1979 and 1985 at Asal (Hofton & Foulger 1996b; Cattin *et al.* 2005b). In the years following the Krafla rifting episode, a number of global positioning system (GPS) surveys were conducted to measure the post-rifting deformation. A network of 40 GPS sites, concentrated within the Krafla volcanic system but extending 130 km

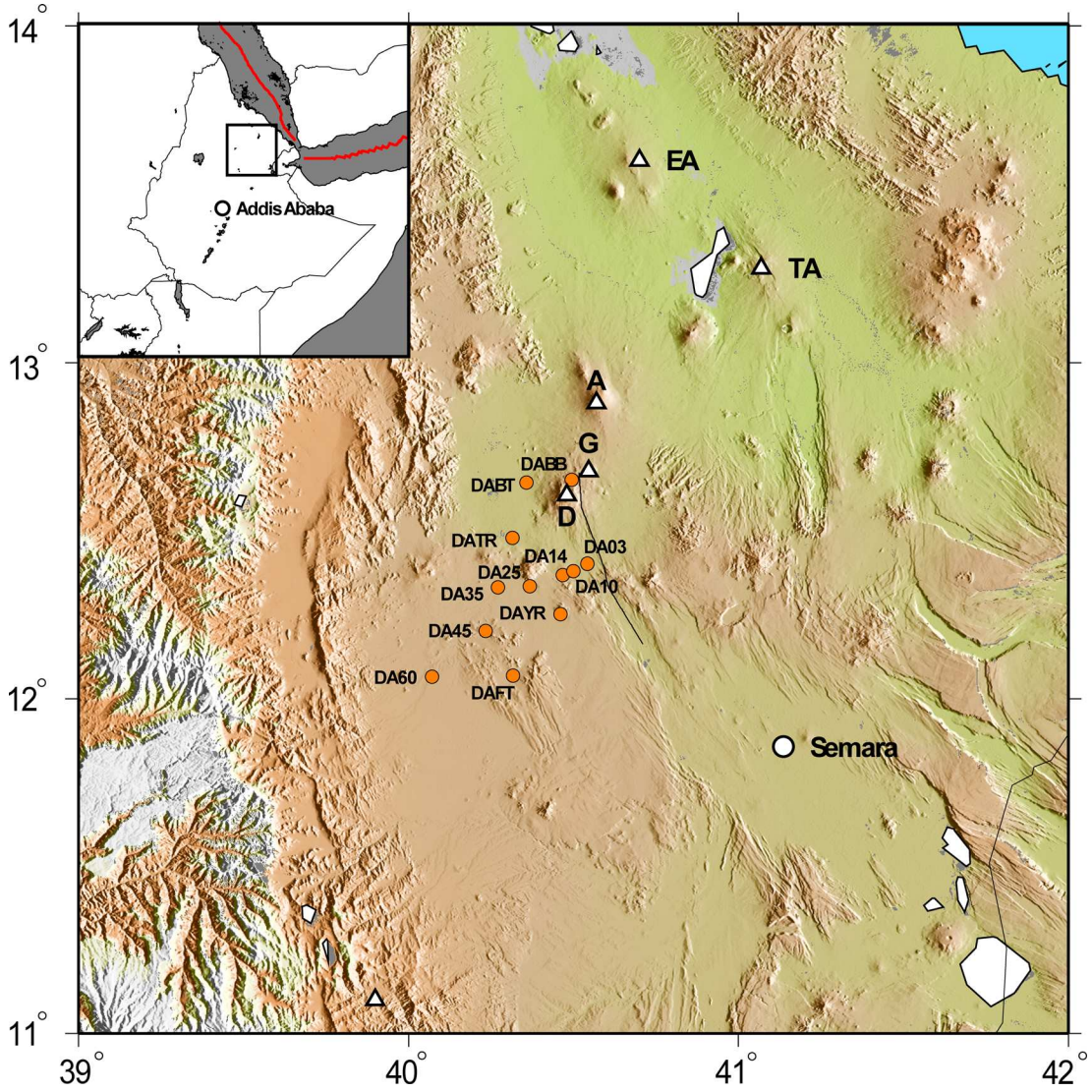

Figure 1. Colour shaded relief map of northern Afar. Main figure shows the location of the dyke (black line) intruded in 2005, Gabho (G), Dabbahu (D), Alayta (A), Ado'Ale (A'A), Tat'Ale (TA) and Erta'Ale (EA) volcanoes (white triangles) and Semara, the regional capital (white circle). Orange circles indicate the continuous GPS stations. The Manda-Hararo segment runs from Dabbahu to Semara.

onto the neighbouring plates, was measured in 1987 and remeasured in 1990. Over this period, the observed increase in the extension rate was explained by transient post-rifting stress relaxation (Foulger *et al.* 1992). There have been a number of attempts to model the stress relaxation signal following the Krafla rifting event using the GPS-derived deformation field (Foulger *et al.* 1992; Hofton & Foulger 1996a,b; Pollitz & Sacks 1996) and more recently using the deformation observed by satellite radar interferometry (InSAR; de Zeeuw-van Dalfsen *et al.* 2004). A model of post-rifting deformation following the Asal rifting episode by (Cattin *et al.* 2005b) incorporated the effect of regional stretching, viscous relaxation, magma intrusion and fault creep to describe rifting processes and concluded that post-rift dyke opening was responsible for most of the observed deformation. Modelling efforts have considered both viscous (Foulger *et al.* 1992) and viscoelastic (Hofton & Foulger 1996a,b) rheologies as well as models based solely on of the movement of magma (de Zeeuw-van Dalfsen *et al.* 2004; Ali *et al.* 2010). Viscoelastic models suggest that relaxation there occurred under a ∼10-km-thick crustal lid in a mantle with a viscosity of $1–3 \times 10^{18}$ Pa s (e.g. Hofton & Foulger 1996a,b).

The ongoing Dabbahu rifting episode began in 2005 September when a ∼60-km-long dyke was intruded along the entire length of the Dabbahu magmatic segment (Northern Manda-Hararo; Wright *et al.* 2006; Ayele *et al.* 2009; Hamling *et al.* 2009; Ebinger *et al.* 2010; Grandin *et al.* 2010a,b; Hamling *et al.* 2010). Since the initial ∼2.5 km^3 dyke intrusion, a further 13 discrete dykes have been detected along the Dabbahu rift segment injecting an additional ∼1 km^3 of new material (Hamling *et al.* 2010; Grandin *et al.* 2010b; Belachew *et al.* 2011). Analysis of InSAR and seismicity data indicate that the 2005 dyke was fed from shallow chambers beneath two volcanoes at the northern end of the segment, Dabbahu and Gabho, and a deeper reservoir at Ado'Ale near the segment centre (Wright *et al.* 2006; Ayele *et al.* 2009). All of the intrusions emplaced following the 2005 September intrusion, between 2006 June and 2010 May, have been fed from Ado'Ale (Grandin *et al.* 2010b; Hamling *et al.* 2010; Belachew *et al.* 2011).

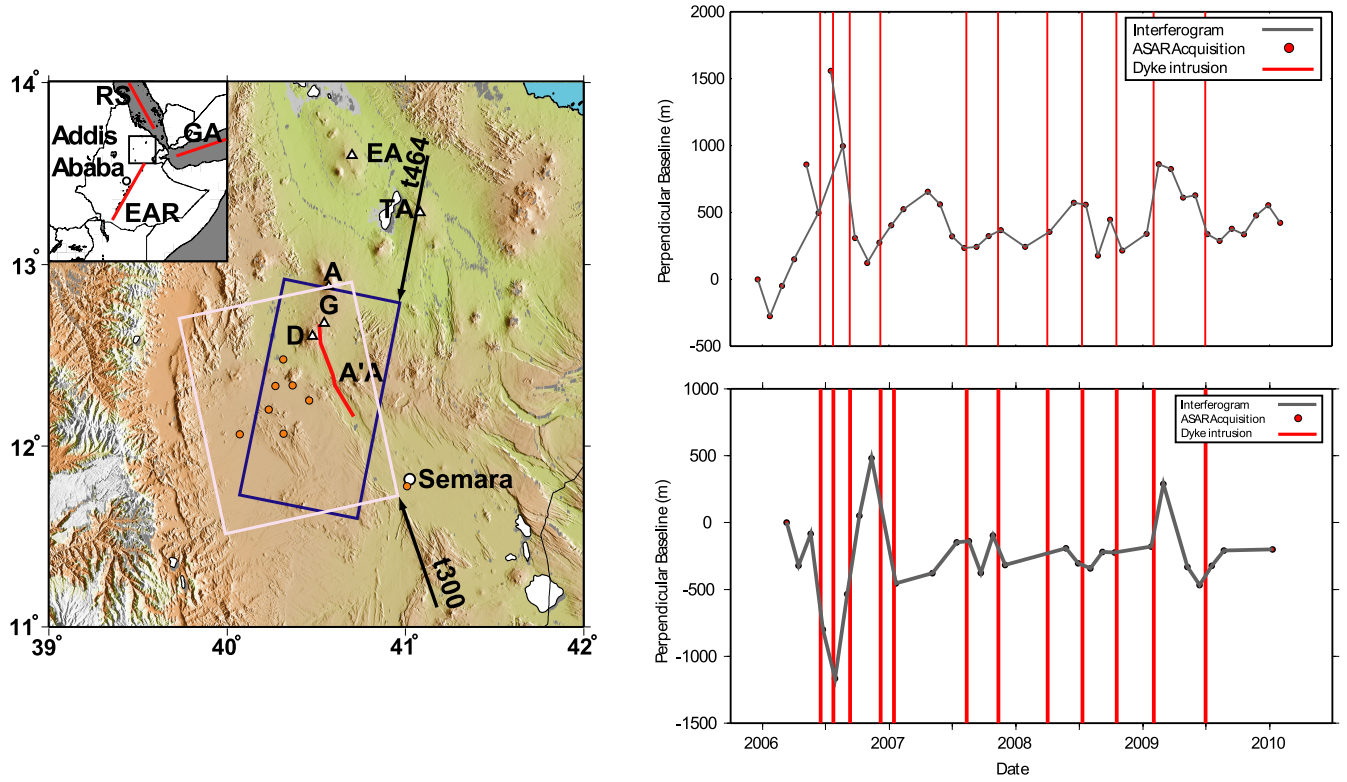

Figure 2. Left: Map of the study area. White and blue boxes show the InSAR coverage for track 300 and 464, respectively. Right: Baseline-time plot for ascending and descending tracks 300 and 464. Grey solid lines represent interferograms formed for this study, red circles represent the ASAR acquisition date and the red lines represent each of the dyke intrusions.

To date, models of the post-rifting deformation following the Dabbahu rifting episode have been either driven entirely by magmatic processes (Grandin *et al.* 2010b) or entirely by viscoelastic relaxation (Nooner *et al.* 2009). Here, we use InSAR observations acquired routinely following the 2005 September rifting events and GPS data collected at continuous sites in the vicinity of the Dabbahu rift to show that viscoelastic relaxation alone is insufficient to explain the observations and present a model that incorporates both magmatic sources and viscoelastic relaxation.

2 METHODS

2.1 InSAR data analysis

InSAR is a widely used technique for monitoring deformation of the Earth's surface. By differencing the phase from two radar images acquired at different times, maps of range change between the radar and ground can be obtained with millimetric precision and centemetric accuracy (Massonnet & Feigl 1998). Following the 2005 September rifting episode regular ASAR (advanced synthetic aperture radar) images have been acquired over the Dabbahu magmatic segment using ESA's Envisat satellite. We use 39 images collected on ascending track 300, to produce 38 interferograms, and 27 images on descending track 464 producing 26 interferograms (Fig. 2). All of the interferograms have been processed using the JPL/Caltech ROI_PAC software (Rosen *et al.* 2004). Topographic corrections were made using a 3 arc-second (90 m) digital elevation model generated by the NASA Shuttle Radar Topography Mission (Farr & Kobrick 2000). Interferograms were filtered using a power spectrum filter (Goldstein & Werner 1998) and unwrapped using the branch cut algorithm (Goldstein *et al.* 1988). The unwrapped interferograms were checked for any unwrapping errors and corrected where necessary. In cases where ambiguities could not be reliably determined, we deleted the ambiguous phase from the unwrapped interferograms.

Using ascending and descending data, which cover the Dabbahu rift segment, we compute two displacement time-series. A total of 64 interferograms were used in the analysis. Before computing the time-series, all of the interferograms have been resampled to give 360 m pixels to reduce the number of data points for the inversion. The first acquisition on track 300 taken after the 2005 September dyke intrusion was on 2005 December 19. Additional images were, in general, acquired every 35 d giving a total of 38 interferograms from 39 epochs between 2005 December and 2010 February (Fig. 2). On track 464 a total of 26 epochs were collected from 2006March 12 to 2010 May 20 (Fig. 2).

Table 1. The rms misfits between displacements measured by InSAR and GPS for tracks 300 and 464.

Station name	DA25	DA45	DAFT	DAYR	DA35	DA60	DABT	DATR
Track 300 misfit (mm)	30	23	11	20	23	21	23	19
Track 464 misfit (mm)	19	15	14	10	20	N/A	13	14

2.2 InSAR analysis of post-rifting deformation in Afar

In a first step, we calculate the surface displacement at each time step, for both ascending and descending data, relative to the first epoch such that:

$$\mathbf{T}\mathbf{d}_{\mathrm{los}} = \mathbf{p} \tag{1}$$

where $\mathbf{p}$ is a vector containing the phase value for each interferogram at each coherent pixel, $\mathbf{T}$ is a matrix containing the time-spans for each of the interferograms and $\mathbf{d}_{\mathrm{los}}$ is the velocity between each epoch which, multiplied by the time interval gives the displacement at each epoch. The inversion is weighted using a variance–covariance matrix (VCM) accounting for atmospheric noise in each interferogram and the correlation between them (Biggs *et al.* 2007). To reduce the effects of the atmosphere, many InSAR studies incorporate a smoothing constraint into the inversion (e.g. Schmidt & Burgmann 2003). This, however, is based on the assumption that the deformation is smooth through time. In this study, where there have been a number of additional dyking events (Hamling *et al.* 2009; Ebinger *et al.* 2010; Grandin *et al.* 2010a,b; Hamling *et al.* 2010), the assumption of steady state deformation breaks down. If smoothing were applied, any offset caused by a dyke intrusion would be smoothed between the epochs on either side of the intrusion event. Therefore, we perform the temporal adjustment without any smoothing.

2.2.1 Comparison with GPS displacements

To validate the results from the InSAR time-series analysis we compare the displacements from InSAR data with those derived from GPS. For each of the GPS stations shown in Fig. 1 we convert the displacements into the satellites line-of-site and extract the displacement from the InSAR time-series at pixels co-located with, or near by, each of the GPS stations. The rms misfit between the displacements calculated by InSAR and GPS is less than 30 mm (Table 1) and, with the exception of pixels on the two northern volcanoes, show an approximately linear displacement with time, consistent with the GPS. Some differences between the InSAR and GPS will arise due to the difference in the reference point and any residual orbital errors in the InSAR data. All of the GPS displacements are calculated with respect to stable Nubia. The InSAR displacements on the other hand are relative to a reference pixel within the interferometric scene.

2.2.2 Estimating background displacement rate from InSAR

In order to determine the background displacement rate around the Dabbahu rift, associated with the 2005 intrusion, we need to take into account the 13 smaller dyke intrusions emplaced following the initial intrusion. Initially, we solve for a single displacement rate and static offsets in the displacement time-series to account for each of the dyke intrusions. However, both the InSAR and GPS displacements suggest that there is a change in the displacement rate in 2006 April (Fig. 3). The change is most notable at GPS in the vicinity of Ado'Ale, whose displacement becomes more perpendicular to the rift after 2006 April (Fig. 3). The change may be the result of a decrease in the inflation at Ado'Ale and/or a switch from predominantly magmatic deformation in the early stages after the 2005 September dyke to viscoelastic relaxation. By solving for two displacement rates find we that the rms misfit is reduced by up to 50 per cent for both the ascending and descending tracks. Therefore, the displacement, at each pixel, at time t is then given by

$$\begin{cases} u_t = r_1(t - t_0) + d1 * H(t - t_{d1}) + \cdots di * H(t - t_{di}) & t \leq t_{r_1} \\ u_t = r_1(t_{r1} - t_0) + r_2(t - t_{r_1}) + d1 * H(t - t_{d1}) + \cdots di * H(t - t_{di}) & t > t_{r_1}, \end{cases} \tag{2}$$

where u_t is the displacement at time t, r_1 is the displacement rate before 2006 April, t_0 is the date of the 1st acquisition. H is a heaviside step function, di is an offset to account for each of the ith dyke intrusions at time t_{di}, r_2 is the displacement rate after 2006 April, and t_{r_1} is the reference time of the 1st acquisition after the rate change. The inversion is weighted using the data VCM, Σ, such that

$$\mathbf{A}^T \Sigma^{-1} \mathbf{A} x = \mathbf{A}^T \Sigma^{-1} \mathbf{b}, \tag{3}$$

where the design matrix, $\mathbf{A}$, contains the times relating to the different displacement rate intervals and steps relating to each of the subsequent dyke intrusions and $\mathbf{b}$ is a matrix containing the displacements at each pixel for each epoch.

The results of the inversion are plotted in Figs 4–6. The spatial pattern of deformation is similar in both intervals with peak displacement rates occurring in the centre and to the southeast of the rift segment (Fig. 4). In the ascending track, prior to the change in the displacement rate, rapid inflation was observed at Gabho at a rate of ∼40 cm yr^{-1} in the satellite's line-of-sight. Pixels located close to Ado'Ale, where both uplift and westward motion was observed, show displacement rates of ∼45 cm yr^{-1} while to the southeast a broad (∼30 km) zone was subsiding at a rate of ∼25 cm yr^{-1}. Far-field velocities at pixels co-located with GPS stations DA25, DAFT and DA60 all show movement away from the satellite during the first interval. The formal 1-σ uncertainty for the ratemap are 9.9 mm yr^{-1} and 9.8 mm yr^{-1} for the first and

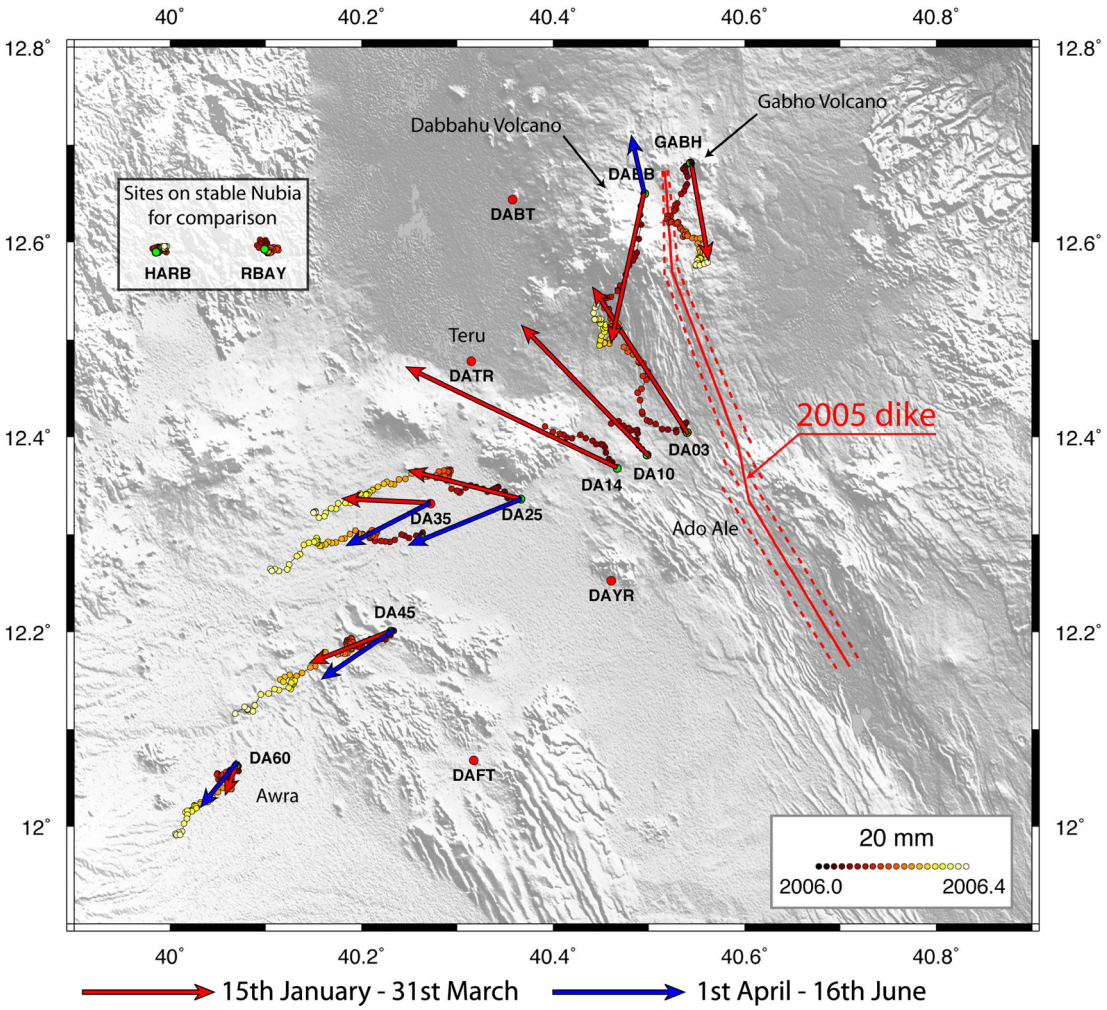

Figure 3. Positions (coloured circles) and displacements measured at nine continuously operating GPS stations during 2006 January–May time interval shown with respect to the Nubian plate. Inset shows the positions of two continuous sites on stable Nubia (Hartebestoek and Richards Bay in South Africa) to illustrate the noise scatter in the measurements for that time interval. Red arrows are for the time interval from January 15 to March 31, blue arrows are for April 1 to June 16. GPS stations DA03, DA10 and DA14 stopped operating on March 27, February 19 and February 28, respectively. Note (1) the radial displacement pattern for the first time interval (with rift-parallel displacements at stations DA03, DA10 and DA14, closed to the 2005 September dike intrusion), consistent with the inflation of a magma source under the Ado'Ale volcanic complex, (2) the kink in the position track at sites DA25 and DA35 in early April, indicative of the slowing down of that inflation.

second intervals, respectively, with errors of ∼8 mm for each of the steps associated with the dyke intrusions. The loss of coherence in the later time intervals, especially in the vicinity and to the west of the rift axis, is a result of the 2006 June dyke intrusion. Unfortunately, due to the acquisition dates on decending track 464, we cannot solve for the displacement rate prior to the change in 2006 April.

After 2006 April, peak displacement rates in the near field slow to ∼20 cm yr^{-1} (e.g. SADA, Fig. 4), similarly the rate of subsidence in the southeast also decreases to ∼14 cm yr^{-1}. Conversely, pixels away from the rift axis show an increased displacement rate, consistent with GPS observations, at rates of between ∼3.5 and 1.4 cm yr^{-1} at points located 25 (DA25) and 45 km (DA45) away from the 2005 September dyke plane, respectively. As with the ascending track, the displacement time-series for the descending track is consistent with GPS (Table 1). Peak displacement rates are found close to the rift axis near the Ado'Ale volcanic complex. The formal $1-\sigma$ uncertainty for the displacement rate is 12.2 mm yr^{-1}.

In addition to the large displacement rates observed around the rift axis, the additional dyke intrusions have resulted in large displacements along the southern section of the rift segment (Figs 5 and 6). Individual intrusions result in offsets of up to ∼750 mm (Fig. 5), summing all of the intrusions gives a maximum displacement of ∼2400 and ∼2800 mm in the vicinity of Ado'Ale on tracks 300 and 464, respectively. The amount of deformation, as a result of these intrusions, is considerable. Although individually, these intrusions are small relative to the 2005 September event their combined post-dyking deformation may be large. An earlier study by Nooner *et al.* (2009) used horizontal GPS displacements from around the Dabbahu rift segment to model the viscoelastic response from the 2005 September event. However, Nooner *et al.* (2009) use the InSAR derived elastic dislocation models of Hamling *et al.* (2009) to remove offsets caused by each of the smaller intrusions, which include 35 d of post-rifting deformation. Using the method described in this paper, where we simultaneously solve for the static shift associated with each dyke and the post-rifting signal, allows us to isolate the 2005 September post-intrusion, steady deformation.

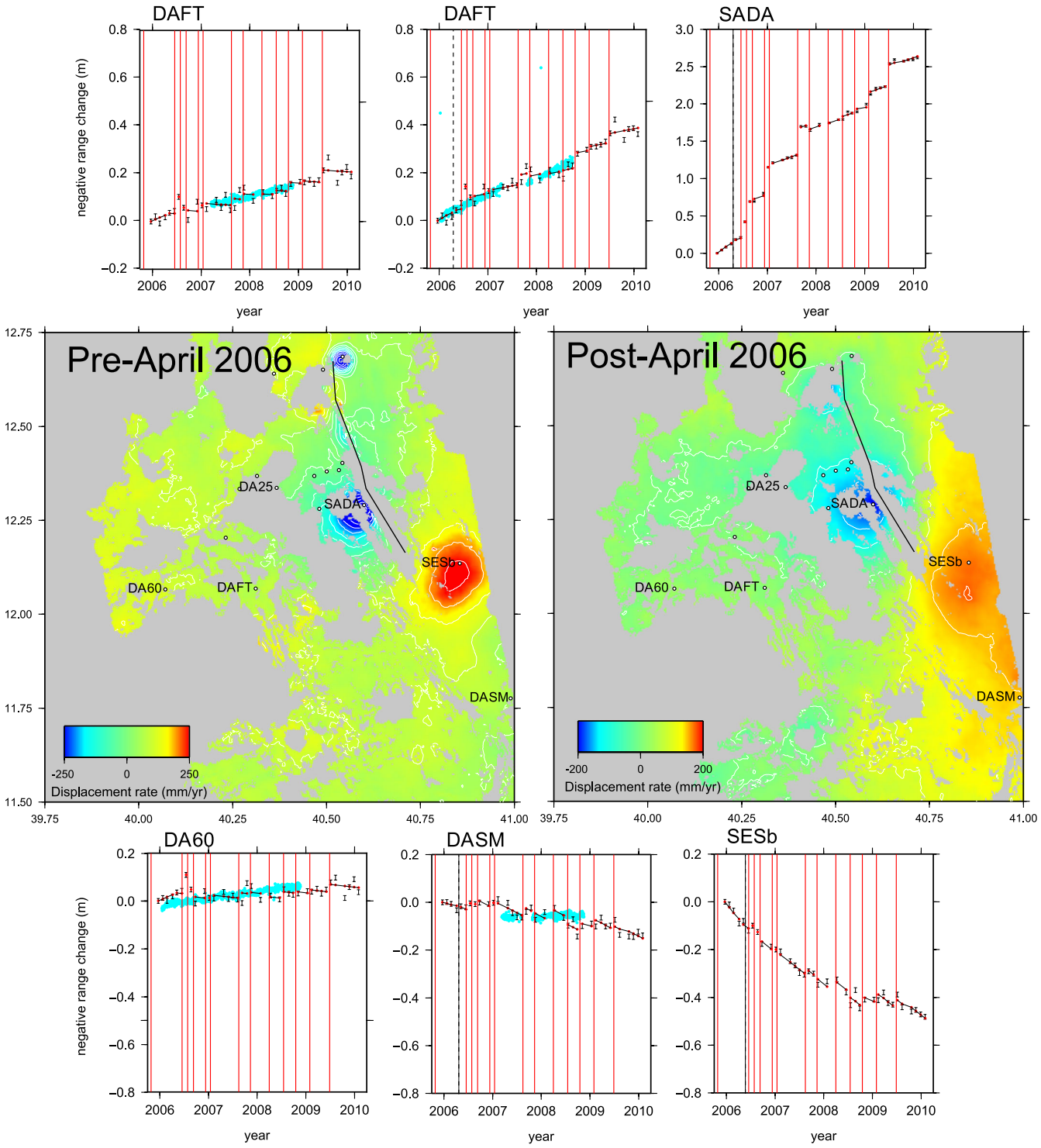

Figure 4. Displacement rates calculated using InSAR data from track 300 for the pre- and post-April 2006 intervals. Main figures show the displacement rates for all coherent pixels between 2005 December and 2006 April (left) and between 2006 May and 2010 February (right), blue colours indicate motion towards the satellite. White circles show the location of GPS sites around the rift segment. Time-series for sites DA60, DAFT, DA25, SADA, SESb and DASM are plotted around the main figure. Blue dots show the displacements calculated by GPS, red lines indicate dyking events, black bars are the displacements estimated from InSAR and red dots and black lines are the predicted displacements from the inversion described above. The black dashed line marks the change in the displacement rate around 2006 April.

2.3 Separating horizontal and vertical deformations

To ease interpretation of the data, we reproject the ascending and descending range change rates, $r_{a,d}$, into equivalent rift-perpendicular, $u_{r\perp}$, and vertical components, u_z. To do this, we assume that there are no displacements parallel to the rift and solve the following equation using

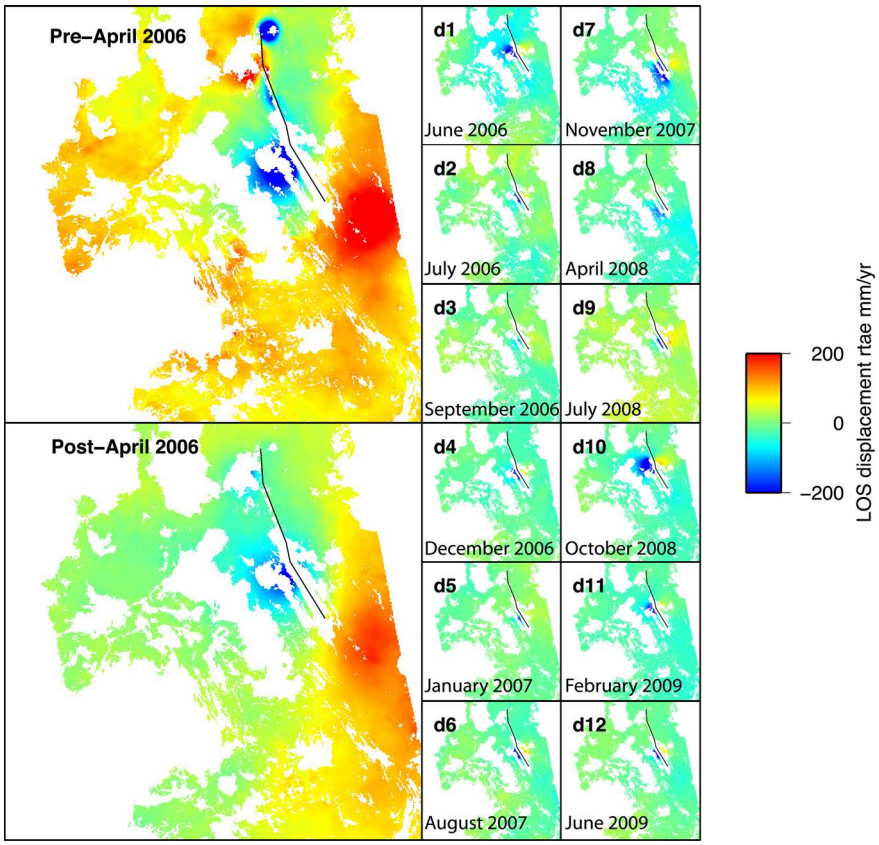

Figure 5. Line-of-sight displacement rates calculated using InSAR data from track 300 for the pre- and post-April 2006 intervals and static displacements caused by each of the subsequent 12 dyke intrusions. The two panels on the left show the displacement rates for all coherent pixels between 2005 December and 2006 April (top) and between 2006 May and 2010 February (bottom), blue colours indicate motion towards the satellite. The two right-hand columns show the static offsets caused by each of the dyke intrusions.

a least squares inversion, weighted using the inverse of the VCM constructed from the errors for the individual displacement rates on the ascending and descending data sets:

$$\begin{pmatrix} \cos\theta_s \hat{s}_{xd} + \sin\theta_s \hat{s}_{yd} & \hat{s}_{zd} \\ \cos\theta_s \hat{s}_{xa} + \sin\theta_s \hat{s}_{ya} & \hat{s}_{za} \end{pmatrix} \begin{pmatrix} u_{r\perp} \\ u_z \end{pmatrix} = \begin{pmatrix} r_d \\ r_a \end{pmatrix}, \tag{4}$$

where $\hat{s}_x$, $\hat{s}_y$ and $\hat{s}_z$ are the three components of the unit vector pointing from the ground to the satellite for the ascending ($_a$) and descending ($_d$) orbits, and θ_s is the angle between the rift segment and north ($\sim 25^\circ$).

The horizontal and vertical components of the deformation can only be retrieved for pixels that are coherent in both ascending and descending data sets. Because of the northward motion shown in the GPS data before 2006 April, we only use data acquired after this time. The calculated displacement rates represent the total rift perpendicular and vertical rates, assuming the linear rates calculated earlier for this interval with all of the dyking events removed, between 2005 May and 2010 February relative to a reference pixel in the south west of the scene. In a final step, we compare GPS measurements recorded over the same interval with the InSAR derived vertical and rift perpendicular rates. For the rift perpendicular displacements, a good agreement is found between InSAR and GPS without adjustment, with all of the co-located GPS displacements falling within the error bounds of the InSAR rates (9 mm yr^{-1}). In the vertical, we find a large difference between the GPS and InSAR. This is likely a result of the difference in reference frame, the GPS are referenced to stable Nubia while the InSAR displacements are relative to a pixel in the southwest of the rift segment. Additionally, any rift parallel displacements will be mapped into the calculated vertical displacement. To account for the difference, we solve for the best fitting offset between the GPS and InSAR data (Fig. 7). After applying the correction, an offset of 59 mm, we find that the rms difference between GPS and InSAR vertical displacement rates is reduced from 61 to 14 mm yr^{-1} (Fig. 7).

Deformation is concentrated around the rift segment with the largest displacements occurring in the vicinity of Ado'Ale. Rift perpendicular displacement rates range from $\sim$135 mm yr^{-1} $\pm$ 17 west of the rift axis to $\sim$180 mm yr^{-1} $\pm$ 17 in the east with peak displacement rates occurring $\sim$20 km from the rift axis (Fig. 8) as shown by Wright *et al.* (2012). Horizontal rates north of Ado'Ale are generally smaller with $\sim$20–30 mm yr^{-1} observed over the observation period. Uplift is observed along most of the rift segment over a broad $\sim$50 km zone. A peak displacement rate of $\sim$240 mm yr^{-1} $\pm$ 9 is observed around Ado'Ale and, to the southeast of the segment, subsidence rates of approximately 80 mm yr^{-1} are observed (Fig. 8). However, due to the viewing geometry of the descending track this mostly falls outside of

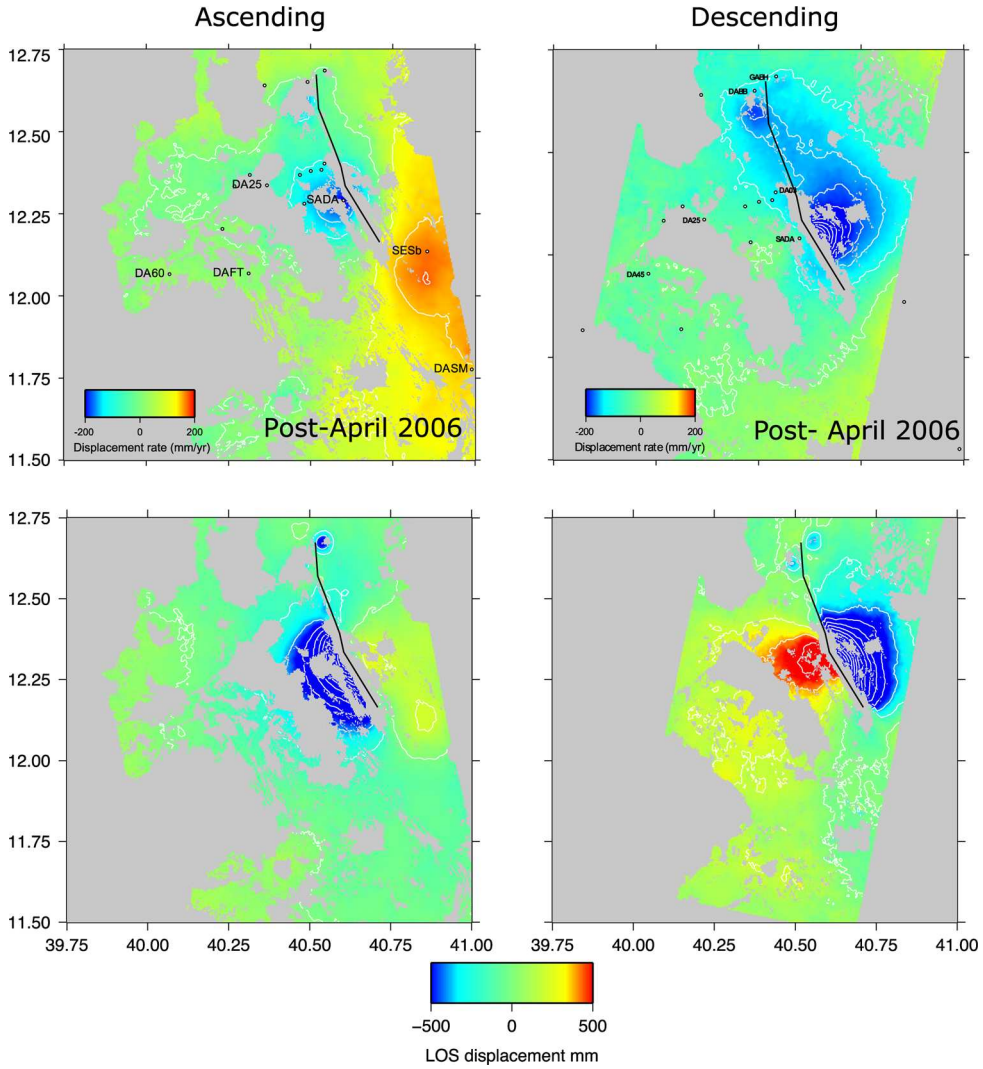

Figure 6. Line-of-site displacement rates and total displacements for all of the dyke intrusions emplaced since 2006 June. Top left: Line-of-sight displacement rate for track 300 from 2006 April to 2010 February. Top right: Line-of-sight displacement rate for track 464 from 2006 April to 2010 February. Bottom left: Dyke displacement for ascending track 300. Bottom right: Dyke displacements for descending track 464. Black line shows the location of the rift axis. White lines are displacement contours at 200-mm intervals.

the scene. North of Ado'Ale there uplift along the rift axis is observed with maximum displacement rates of 100 mm yr^{-1}. Uplift is also observed at Gabho and Dabbahu volcanoes at rates of ∼70 and 150 mm yr^{-1}, respectively.

3 MODELLING OF POST-RIFTING DEFORMATION IN AFAR

We use a two-layered, semi-analytic, elastic-viscoelastic model (Fukahata & Matsu'ura 2005, 2006; Hashima *et al.* 2008). The code computes the viscoelastic deformation resulting from a finite rectangular dislocation. Each layer is assumed to be isotropic, homogeneous and either elastic or viscoelastic with the viscoelastic rheology being Maxwell in shear and elastic in bulk.

3.1 Model configuration

We use two source models. Each is composed of six 10 km segments extending from 1 to 9 km depth, based on the mean opening along the 2005 September dyke given by Wright *et al.* (2006), Hamling *et al.* (2010) (Fig. 9), but the second model also includes Mogi sources to represent known magmatic bodies around the rift axis. For all of the model calculations we use the depth averaged elastic parameters derived from seismic and gravity data (Makris & Ginzburg 1987; Tiberi *et al.* 2005, Table 2) for both the elastic and viscoelastic layers.

Using the parameters shown in Table 2 and the opening distribution shown in Fig. 9, we generate a set of forward models with different elastic lid thicknesses (10–30 km) and viscosities (10^{17}–10^{19} Pa s) and compare the results with the rift perpendicular and vertical

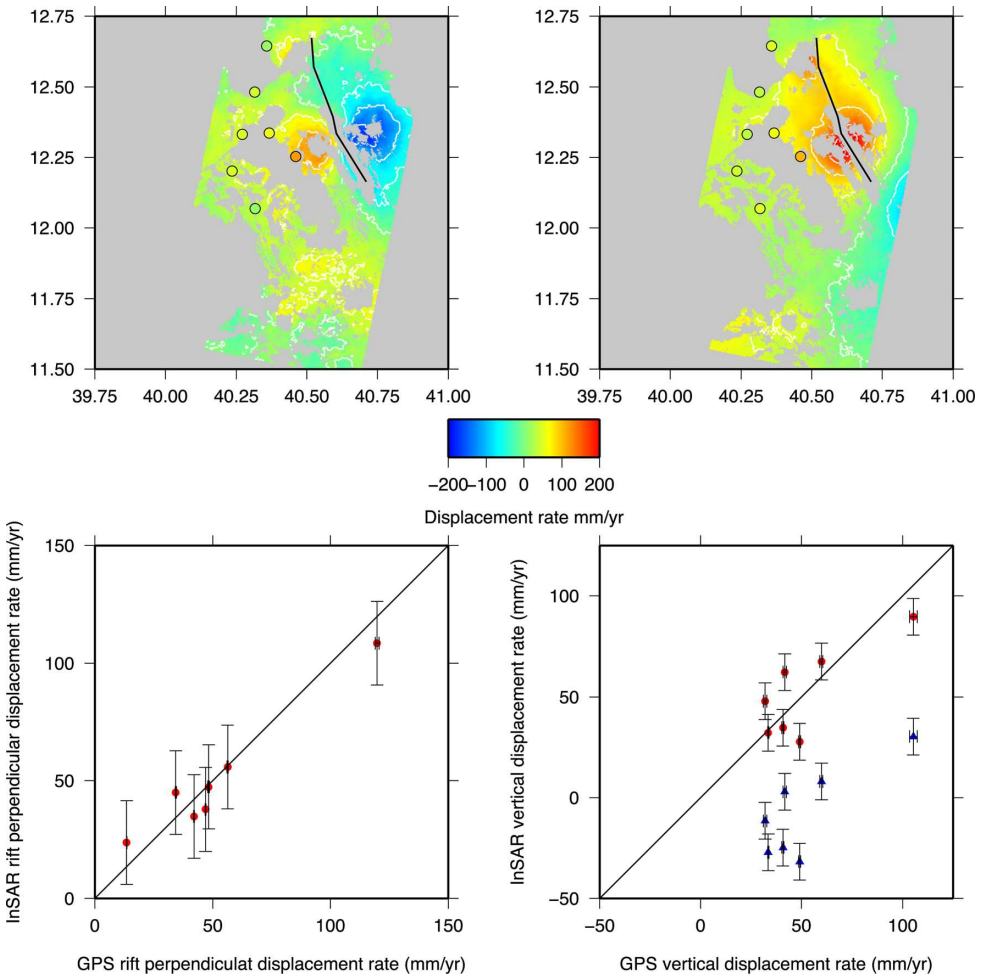

Figure 7. Comparison between rift perpendicular and vertical displacement rates calculated using InSAR and GPS from 2006 April to 2010 February. Top left: Rift perpendicular displacement rate calculated using InSAR with GPS site displacements projected onto map. Top right: Vertical displacement rate calculated using InSAR with GPS site displacements projected onto map. Bottom left: Correlation between the rift perpendicular displacement rates calculated by InSAR and GPS with error bars. Bottom right: Correlation between the vertical displacement rates calculated by InSAR and GPS with error bars. Blue triangles show the correlation before correcting the InSAR by applying a static shift.

displacements by calculating the root mean square misfit 1, 2 and 3.5 yr after the change in rate in 2006 April. First, we assume that all of the observed deformation is a result of viscoelastic relaxation with no magmatic contribution.

To find the best fitting model we calculate the total misfit by summing the misfits for the rift perpendicular and vertical displacements with equal weight (Fig. 10). For the rift perpendicular displacements there is strong trade-off between lid thickness and viscosity. Similar misfits are found with either a thick lid (19–30 km) and a lower viscosity (10^{18} Pa s) or a thin lid (10–13 km) with a higher viscosity of $10^{18.5}$ Pa s. For all times, we find a best fitting viscosity of 10^{18} Pa s for the vertical displacements. However, the thickness of the elastic lid is poorly constrained with thicknesses of 23–30 km giving similar misfits.

The residual plots shown in Fig. 11, taken after 3.5 yr, highlight a number of deforming areas around the rift segment which cannot be explained by this simple viscoelastic model (elastic lid—21 km, viscosity—10^{18} Pa s). Rift perpendicular displacements are underestimated close to Ado'Ale and to the north and south of the rift segment. The vertical displacements are also, in general, underestimated. Large residuals occur around the Ado'Ale volcanic complex, to the southeast of the rift segment and to the west of the rift axis in the far field.

To improve the fit to the data, and to account for the various magmatic sources located around the rift segment, we next include an inversion for four sources beneath Gabho, Dabbahu, Ado'Ale and to the south east of the segment (Mogi 1958). First, we subtract each of the viscoelastic models, shown in Fig. 10, away from the data. We then use the residuals to invert for the volume changes at each of the sources. The depth of the sources beneath Gabho, Dabbahu and Ado'Ale have been fixed at 4, 4 and 10 km as suggested by previous studies (e.g. Wright *et al.* 2006; Grandin *et al.* 2009; Hamling *et al.* 2009). For source to the south east of the segment, we vary the depth between 15 and 25 km and assess the rms misfit at each depth interval. The minimum misfit is found at 17 km. With the depth of each source fixed, the change in volume, at each source, can be determined by performing a simple least-squares inversion. Once the volume of the sources is found we remove the magmatic deformation from the data and recalculate the viscoelastic model. This process, of removing the viscoelastic and magmatic components, is repeated until the solution converges.

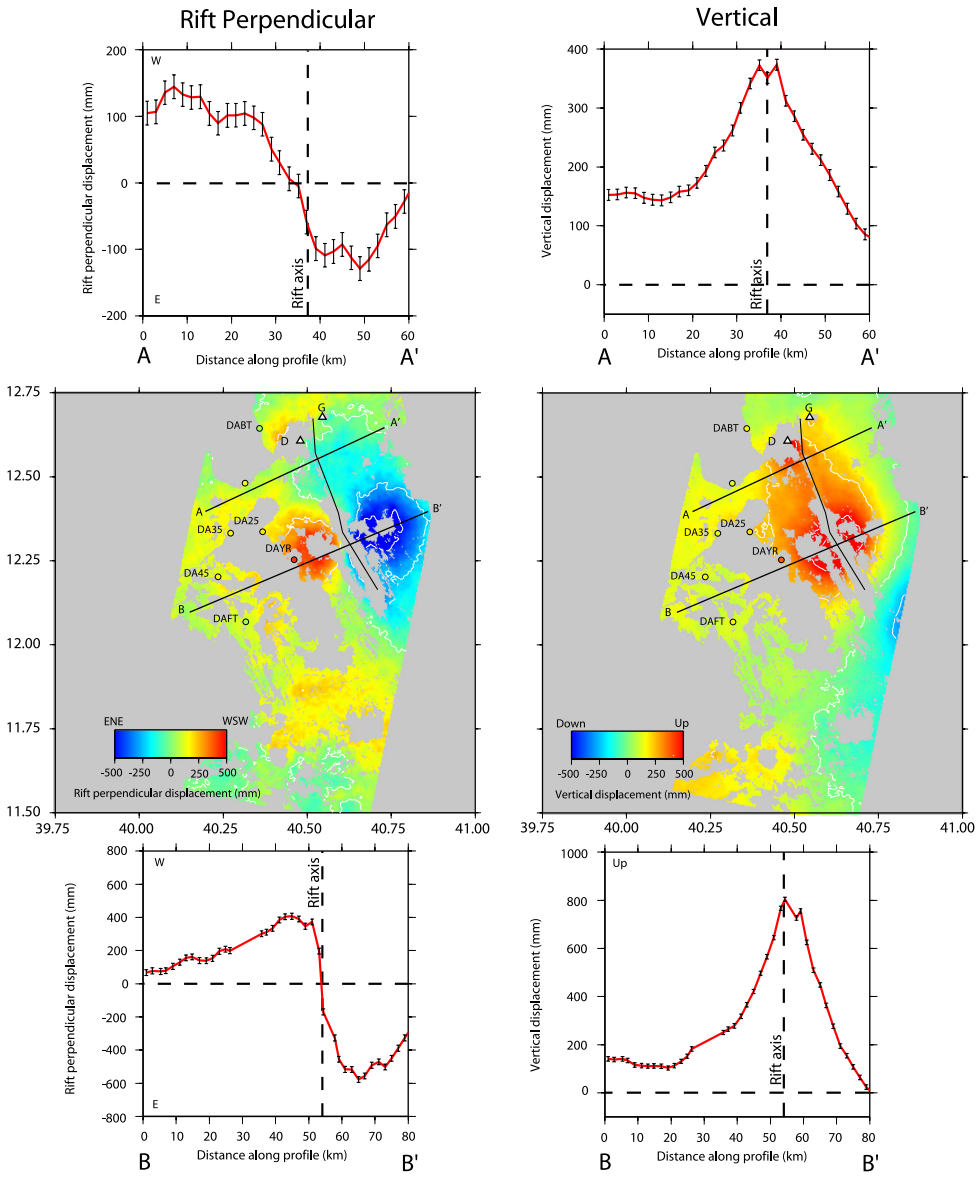

Figure 8. Rift perpendicular and vertical displacements between 2006 June and 2010 January. White triangles represent Dabbahu (D) and Gabho (G) volcanoes, white circles show the location of GPS sites around the rift segment. Top and bottom: Displacement profiles along A-A′ and B-B′.

As before, we assess the rms misfit for the rift perpendicular, vertical displacements and the total misfit after 1, 2 and 3.5 yr (Fig. 12). The best fitting model is found with an elastic lid thickness of between 15 and 30 km and a viscosity of $10^{18.5}$. Our inversion finds volume changes of 0.13 and -0.08 km^3 yr^{-1} at Ado'Ale and at the source to the south east and 0.0063 and 0.0020 km^3 at Dabbahu and Gabho. This gives an rms misfit of 97, 95 and 192 mm to the rift perpendicular, vertical and total displacements, respectively, after 3.5 yr.

Despite the improved fit to the data there are still large differences after inclusion of the magmatic sources (Fig. 13). In general, the model is able to approximate the wavelength of the rift perpendicular displacements (A-A′ and B-B′ in Fig. 13). Residuals are found to the north of Dabbahu and Gabho although this signal may not be related to deformation around the rift segment. In the vertical component, there are large differences between the modelled and observed displacements. Even with the addition of the magmatic sources, the model predicts subsidence in the farfield while both InSAR and GPS observations show uplift in this region. As a consequence, the modelled displacements associated with the inflation around Ado'Ale are too large and the model requires a thick lid in order to reduce the amount of subsidence away from the rift axis (B-B′).

4 DISCUSSION

The pattern of deformation around the Dabbahu segment, observed following the 2005 September rifting event, shows a number of features which cannot be explained by viscoelasticity alone. Ignoring the magmatic sources around the rift segment, the best fitting model suggests an elastic lid thickness of 21 km, similar to direct estimates of Moho depth (16–18 km) in central Afar (Dugda *et al.* 2005; Hammond *et al.* 2008,

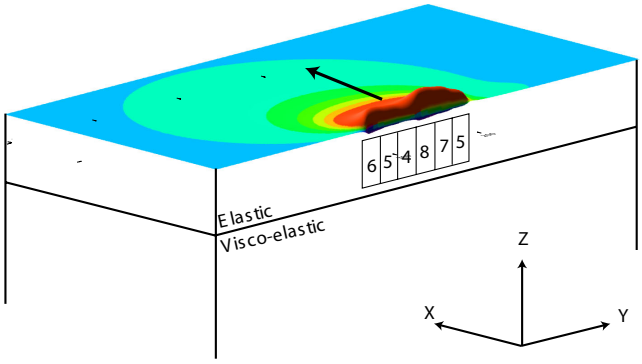

Figure 9. Viscoelastic model setup. Rectangular patches represent dyke opening in the X direction by the amount indicated at the centre of each patch in metres.

Table 2. Elastic and viscoelastic properties used in the model.

Layer	V_p (km s^{-1})	V_s (km s^{-1})	Poisson ratio	Youngs modulus (GPa)	Density (kg m^{-3})
Elastic	5.35	2.95	0.28	58	2600
Viscoelastic	7.1	3.7	0.31	108	3000

2009) but much larger than the depth of seismicity and dyke intrusions along the rift segment (Belachew *et al.* 2011). Despite the improved fit to the data there are still differences after inclusion of the magmatic sources (Fig. 13). In general, the model is able to approximate the wavelength of the rift perpendicular displacements (A-A′ and B-B′ in Fig. 13). Residuals are found in the centre of the rift axis close to the Ado'Ale complex, where the model overestimates the deformation. Residuals to the north of Dabbahu and Gabho and to the south of the segment may not be related to the deformation around the rift segment. In the vertical deformation field, there are large differences between the modelled and observed displacements. Even with the addition of the magmatic sources, the model predicts subsidence in the farfield whilst both InSAR and GPS observations show uplift in this region (Fig. 14). As a consequence, the best-fit model probably overestimates

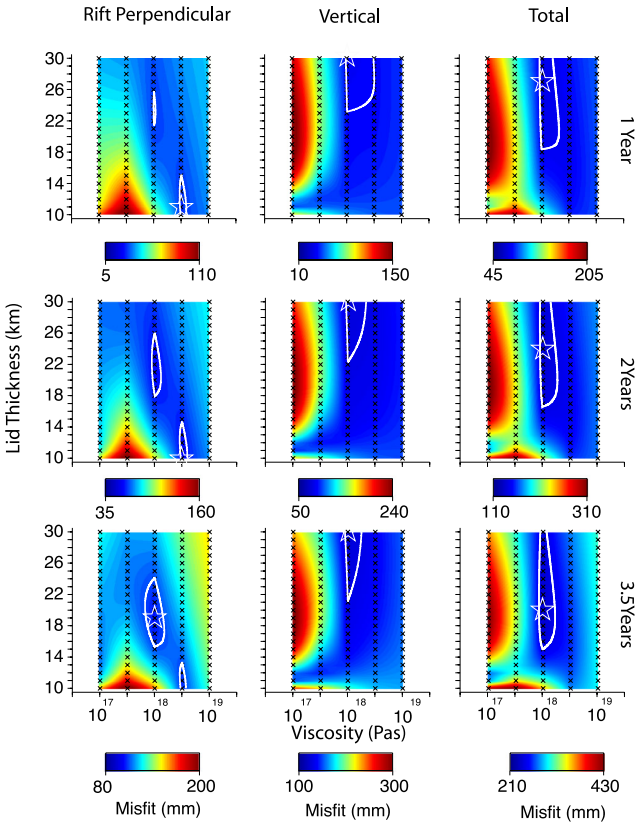

Figure 10. The rms misfit for a range of viscoelastic forward models with varying viscosities and elastic lid thicknesses. Left: Misfit between modelled and observed rift perpendicular displacements. Centre: Misfit between modelled and observed vertical displacements. Right: Misfit between modelled and observed total displacement. In each case the star shows the location of the best fitting model, the white line marks the region of acceptable models based on the minimum misfit plus 5 per cent and the black crosses show the location of the model runs.

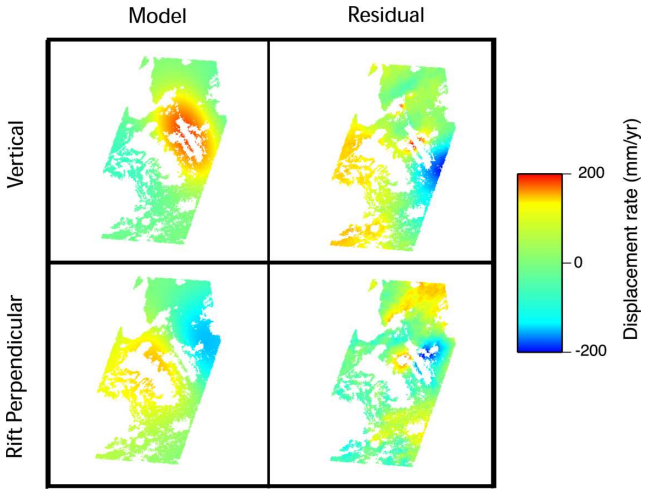

Figure 11. Difference between best fitting viscoelastic model and data after 3.5 yr. The model consists of a 21-km-thick elastic lid overlying a viscoelastic half-space with a viscosity of 10^{18} Pa s. Left: Residual rift perpendicular displacements. Right: Residual vertical displacements.

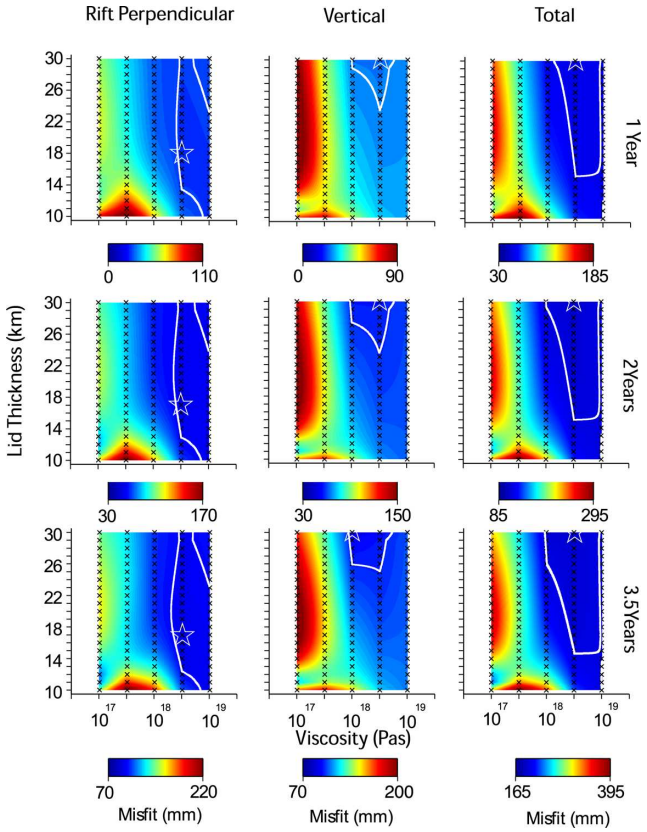

Figure 12. The rms misfit for a range of viscoelastic forward models with varying viscosities and elastic lid thicknesses with magmatic sources included around the rift. Left: Misfit between modelled and observed rift perpendicular displacements. Centre: Misfit between modelled and observed vertical displacements. Right: Misfit between modelled and observed total displacement. In each case the star shows the location of the best fitting model, the white line marks the region of acceptable models based on the minimum misfit plus 5 per cent and the black crosses show the location of the model runs. Each row represents the misfit after 1, 2 and 3.5 yr.

the deformation associated with the inflation around Ado'Ale and suggests a thick lid in order to reduce the amount of subsidence away from the rift axis (B-B′). If we fix the amount of inflation at Ado'Ale to equal to the amount of magma which is removed from the source to the south east of the segment (0.27 km^3), then the residual in the vertical signal, in the vicinity of Ado'Ale, is reduced. However, this has the opposite affect on the rift perpendicular residuals that increase around the Ado'Ale complex. In this model, we do not consider the effect of using a viscoelastic rheology for the post-rifting deformation with an elastic half-space for the point source models. (Bonafede & Ferrari 2009) show that a constant overpressure on a source in a viscoelastic medium produce surface displacements consistent with observations at Camp Flegrei between 1982 and 1984 without the need of additional material being intruded. However, in Afar, where new intrusions have

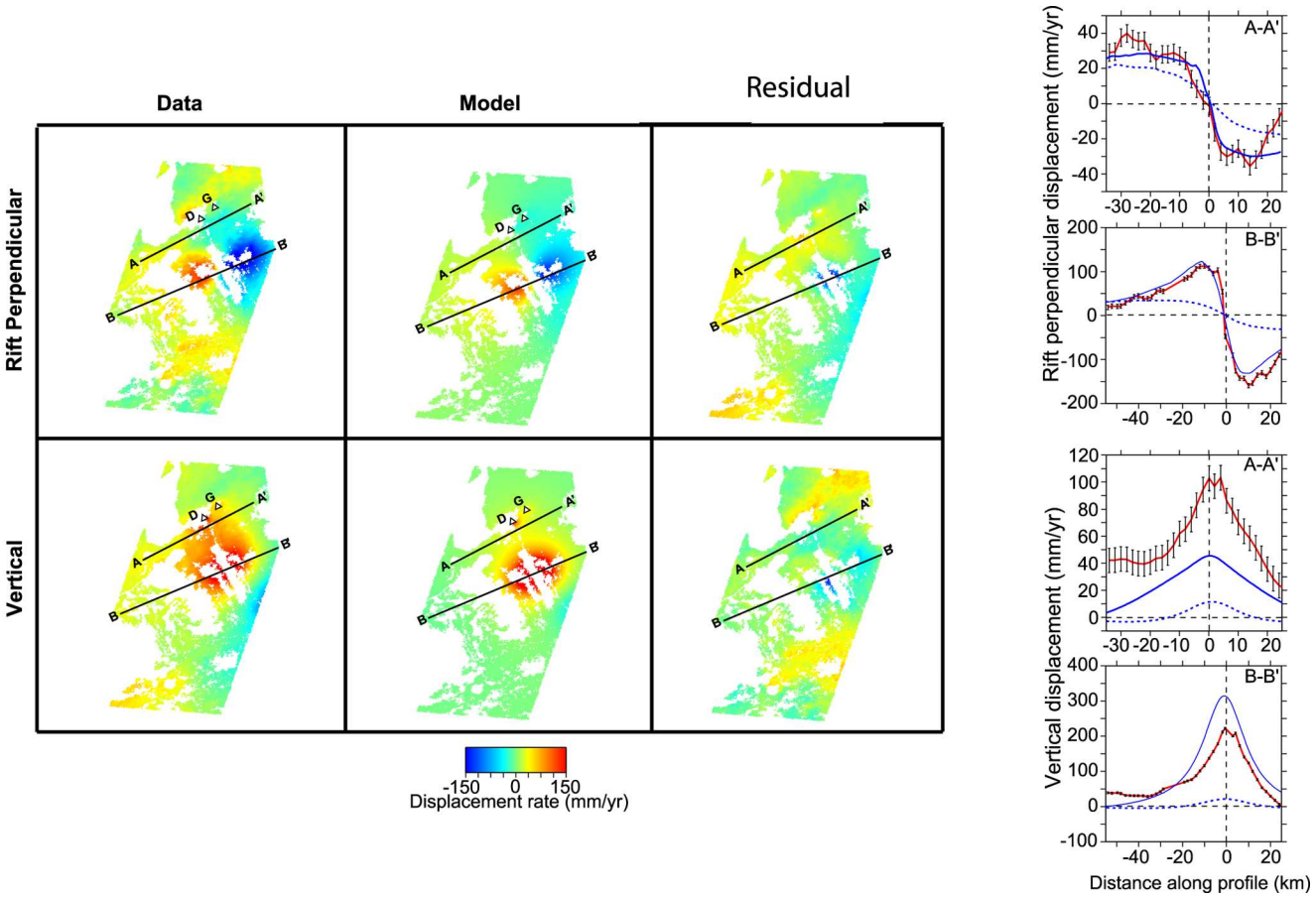

Figure 13. Comparison between observed and modelled rift perpendicular and vertical displacement rates. Left: observed rift perpendicular and vertical displacement rates, centre: modelled rift perpendicular and vertical displacement after 1 yr. Right: Profiles through A-A′ and B-B′. Solid blue line shows the best fit model when magmatic sources are included while the dashed line shows the best fitting model from Nooner *et al.* (2009). Red solid line shows the data with corresponding error bars.

likely been fed, at least partially, by magma from the source at Ado'Ale it is reasonable to assume that there has been continued movement of material at the sources around the rift. Assuming that the magma is supplied at a constant rate, (Bonafede & Ferrari 2009) show that the surface displacement is only weakly dependent on the rheology. In this case, the difference between the surface displacements given by a point source in an elastic half-space and one in a viscoelastic medium would be small.

Despite the simple nature of our source model, we are able to explain the broad patterns of deformation around the rift segment. Some of the differences between our best fit model and the observations will be a result of the simple dyke source we use to represent the 2005 September intrusion. Our model, largely based on the Wright *et al.* (2006) result, has lower amounts of opening along the central and southern sections of the rift compared with the models of Grandin *et al.* (2009) and Ayele *et al.* (2007). By increasing the amount of opening in this region by 2 m, we find that there is very little effect to the viscoelastic response over the observational period. After 4 yr the difference in the peak displacement is 4 mm and we find that the best fit solution gives the same range of viscosities and lid thicknesses. All of the reported opening models for the September intrusion are a result of the inversion of InSAR data and will include a proportion of post-dyke opening. Therefore, we feel that given the errors in the published source distributions, using a model with lower opening is a reasonable estimate of the 2005 September intrusion. This model also assumes uniform opening from 1 to 9 km depth. Published models (Wright *et al.* 2006; Grandin *et al.* 2009, e.g.) show that most of the dyke opening occurred in this range but use a smoothing parameter which acts to taper the opening distribution with depth. However, since the dyke is buried within the elastic halfspace, the effect on the surface displacements caused by tapering of the opening distribution should be minimal. By conserving the same average opening across a segment, but with the distribution tapered such that the maximum opening is at 5 km depth, we find that the difference in the viscoelastic response over 4 yr, assuming our best fit model parameters, is only 2 per cent.

A notable feature of the inversion is that the best fitting models to the horizontal and vertical displacements do not agree. Using only the rift perpendicular displacements results in a thinner elastic lid (∼13 km), similar to that reported by Nooner *et al.* (2009) who modelled horizontal displacements measured by GPS. Also, the predicted volume change at the off axis source is only 10 per cent of that predicted when the vertical deformation is included. Although the model is unable to constrain the elastic thickness when the vertical deformation is included, it does give a lower limit on the thickness of the elastic lid as the magnitude of the uplift along the rift zone strongly depends on the thickness of the lid. In order to generate uplift along the rift axis from viscoelastic relaxation, the thickness of the elastic lid must be at least

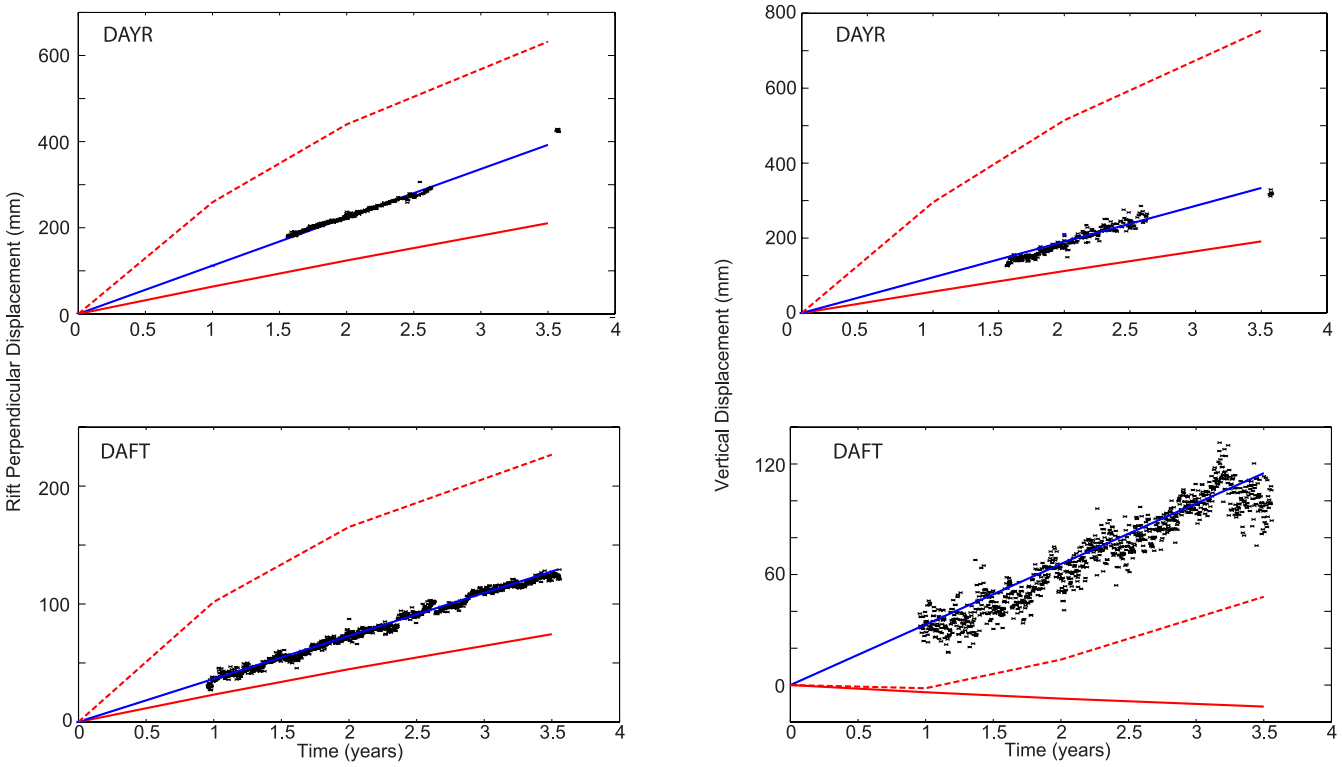

Figure 14. Comparison between observed and modelled rift perpendicular (left) and vertical displacement (right) calculated by InSAR and GPS at DAFT (top row) and DAYR (bottom row). Solid blue lines show the displacements calculated by InSAR, black dots show the displacements measured from GPS. Solid red lines show the modelled displacement assuming a viscosity of $10^{18.5}$ Pa s and an elastic lid of 30 km. Dashed red lines show the modelled displacement from a model with a viscosity of $10^{17.5}$ Pa s and an elastic lid of 30 km.

12 km. Even after including the magmatic sources, the elastic thickness predicted by this model remains substantially larger than previous estimates (e.g. Nooner *et al.* 2009; Belachew *et al.* 2011) but is poorly constrained. The best fitting viscosity of $10^{18.5}$ Pa s, on the other hand, is in agreement with estimates from other subaerial rift segments (Foulger *et al.* 1992; Hofton & Foulger 1996a,b; Pollitz & Sacks 1996; Nooner *et al.* 2009; Pagli *et al.* 2009). Furthermore, the fact that the deformation around the rift segment appears to be linear, at least in the early stages following rifting, requires that the viscosity in the model is larger than 10^{18} Pa s. Below this value there is a large departure from a constant displacement rate (Fig. 14).

Models of continued dyke opening have also been proposed to explain the deformation following major rifting events (de Zeeuw-van Dalfsen *et al.* 2004; Cattin *et al.* 2005b; Grandin *et al.* 2010b). This model was discounted by Nooner *et al.* (2009) as dyke opening would need to occur in the upper mantle to match the observed long wavelength regional post-rifting deformation signal. Grandin *et al.* (2010b) suggest that dyke opening at depths greater than the brittle crustal can occur providing there is sufficient magma to accommodate the tectonic strain. A major difference between the viscoelastic and continued dyke opening models is that the continued opening model predicts subsidence over the dyke with uplift occurring on the flanks of the intrusion. Our analysis suggests that there is uplift along the entire rift axis and, as such, does not support the idea of continued dyking at depth. The asymmetry in the across axis profiles (A-A′ to B-B′) shown in Fig. 13 suggest that the uplift observed in the farfield does not have the same extent on the eastern edge of the segment. A magnetotelluric survey across the central part of the rift suggests that there is a broad, ∼15-20 km, region of conductive material extending to the west of the rift axis beneath this region which could be the cause of the uplift in this region Desissa *et al.* (2009). Given that the horizontal displacements seem to be largely unaffected by the body, it is more likely to be a tabular source such as a sill or, perhaps, underplating of melt.

5 CONCLUSIONS

Using ascending and descending InSAR data, we have calculated the background rift perpendicular and vertical displacement rates resulting from the 2005 September dyke intrusion. The InSAR derived displacements are similar to those given by GPS and suggest that, with the exception of the first 6 months, the inter-dyking surface displacements during the first few years of the post-rifting cycle are near linear. Modelling suggests that viscoelastic relaxation of the stresses induced by the 2005 September intrusion cannot explain the observed post-dyking deformation alone and requires the addition of magmatic sources around the rift. Our best fit model suggests upper mantle viscosities of $1 \times 10^{18-19}$ Pa s, which is in agreement with other subaerial rift systems, and an elastic thickness of 15–30 km. Sources beneath Ado'Ale and to the south east of the segment are predicted to inflate/deflate by $\sim 0.47 \pm 0.008$ and $\sim -0.28 \pm 0.2$ km^3, respectively. Although these

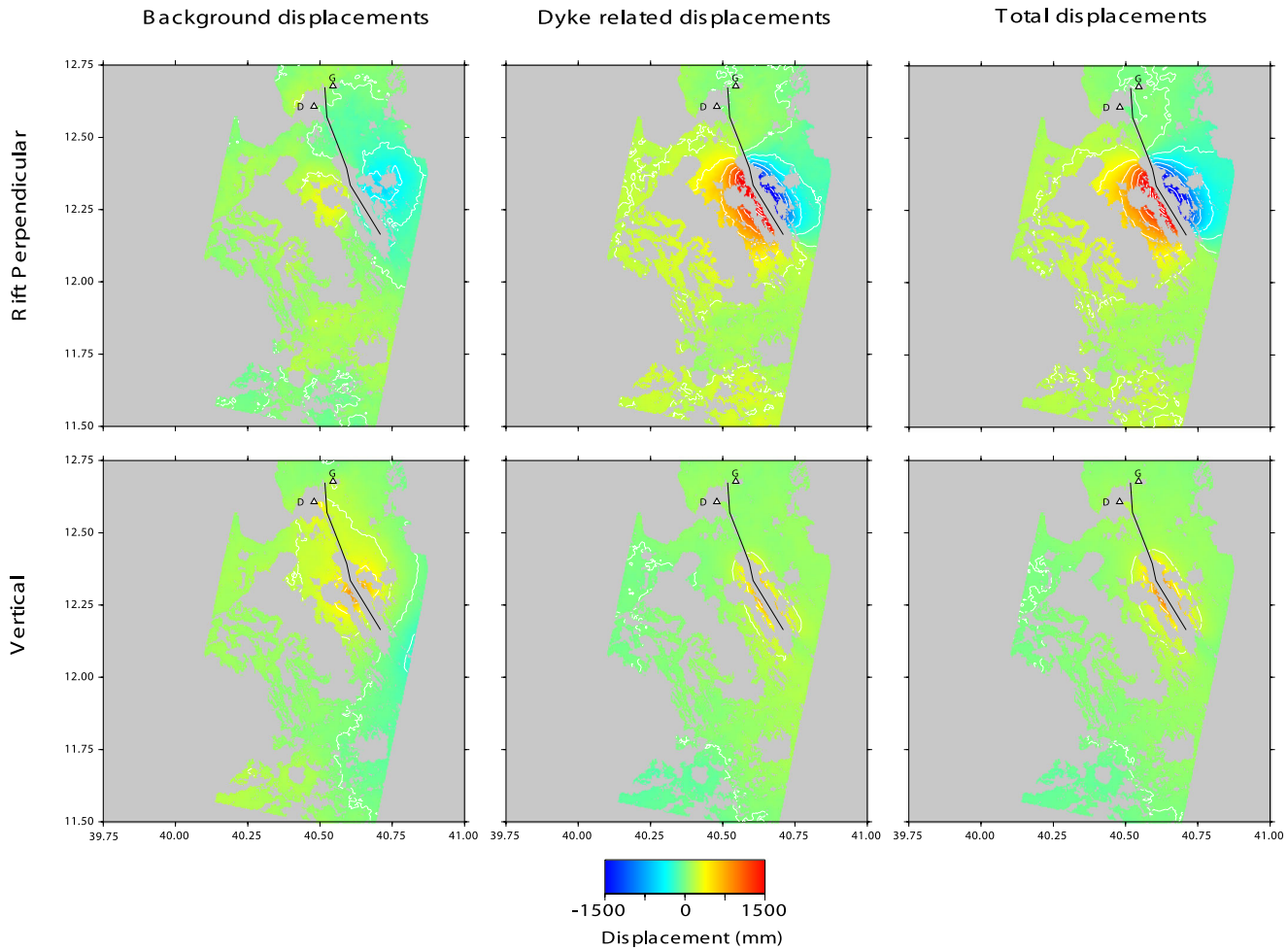

Figure 15. Non-dyke, dyke and total rift perpendicular and vertical displacements between 2006 June and 2010 February. Left: Background rift perpendicular and vertical displacements. Centre: Rift perpendicular and vertical displacements associated whit dyke intrusions between 2006 June and 2010 February. Right: Total residual rift perpendicular and vertical displacements.

data suggest that a large amount of the deformation around the Dabbahu rift segment is related to viscoelastic relaxation and the accumulation of magma beneath the rift axis, this is still only a fraction of that from repeated dyke intrusions along the segment (Fig. 15). Separation of the dyke and non-dyke related displacements indicates that much of the deformation, observed since the 2005 September event, is a result of additional dyke intrusions in the vicinity and to the south of the Ado'Ale volcanic complex. In order to identify the transition from magmatically dominated to viscoelastic deformation, we require a longer observational period and the development of more complex models which can better account for magmatic and viscoelastic processes.

ACKNOWLEDGEMENTS

We would like to thank the Institute for Geophysics, Space Science and Astronomy of Addis Ababa University, the Afar Regional government and the Ethiopian Ministries of Capacity Building, and of Mines and Energy for all their help and support. Our work is supported by NERC grants NE/D008611/1, NE/D01039X/1 and NE/E007414/1, NSF grants EAR-0635789 and EAR-0613651, a NERC-COMET studentship to IJH and a Royal Society University Research Fellowship to TJW. Radar data are from the European Space Agency. We would also like to thank the two anonymous reviewers whose insightful comments have greatly improved the manuscript.

REFERENCES

Abdallah, A. *et al.*, 1979. Relevance of Afar seismicity and volcanism to the mechanics of accreting plate boundaries, *Nature,* **282,** 17–23.

Ali, T., Feigl, K., Thurber, C., Masterlark, T., Carr, B. & Sigmundsson, F., 2010. Geodetic measurements and models of rifting in Northern Iceland for 1993-1998, *AGU Fall Meeting Abstracts,* **1,** 05.

Ayele, A. *et al.*, 2007. The volcano-seismic crisis in Afar, Ethiopia, starting September 2005, *Earth planet. Sci. Lett.,* **255,** 177–187.

Ayele, A. *et al.*, 2009. September 2005 mega-dike emplacement in the Manda-Harraro nascent oceanic rift (Afar depression), *Geophys. Res. Lett.,* **36**(L20306), doi:10.1029/2009GL039605.

Belachew, M., Ebinger, C., Coté, D., Keir, D., Rowland, J.V., Hammond, J.O.S. & Ayele, A., 2011. Comparison of dike intrusions in an incipient seafloor-spreading segment in Afar, Ethiopia: seismicity perspectives, *J. geophys. Res.,* **116,** B06405, doi:10.1029/2010JB007908.

Biggs, J., Wright, T., Lu, Z. & Parsons, B., 2007. Multi-interferogram method for measuring interseismic deformation: Denali Fault, Alaska, *Geophys. J. Int.,* **170,** 1165–1179.

Bonafede, M. & Ferrari, C., 2009. Analytical models of deformation and residual gravity changes due to a mogi source in a viscoelastic medium, *Tectonophysics,* **471**(1), 4–13.

Buck, W.R., Einarsson, P. & Brandsdóttir, B., 2006. Tectonic stress and magma chamber size as controls on dike propagation: constrints from the 1975-1984 Krafla rifting episode, *J. geophys. Res.,* **111,** doi:10.1029/2005JB003879.

Cattin, R., Doubré, C., Chabalier, J.B., King, G., Vigny, C., Avouac, J.P. & Ruegg, J.C., 2005a. Numerical modelling of quaternary deformation and post-seismic displacement in the Asal-Ghoubbet rift (Djibouti), (Africa), *Earth planet. Sci. Lett.,* **239,** 352–367.

Cattin, R., Doubre, C., de Chabalier, J.B., King, G., Vigny, C., Avouac, J.-P. & Ruegg, J.-C., 2005b. Numerical modelling of quaternary deformation and post-rifting displacement in the Asal-Ghoubbet rift (Djibouti, Africa), *Earth planet. Sci. Lett.,* **239,** 352–367.

de Zeeuw-van Dalfsen, E., Pedersen, R., Sigmundsson, F. & Pagli, C., 2004. Satellite radar interferometry 1993–1999 suggests deep accumulation of magma near the crust-mantle boundary at the Krafla volcanic system, Iceland, *Geophys. Res. Lett.,* **31,** 13611.

Desissa, M., Whaler, K., Houtot, S., Dawes, G., Fisseha, S. & Johnson, N., 2009. A magnetotelluric study of continental lithosphere in the final stages of break-up: Afar, Ethiopia, in *Proceedings of IAGA Assembly, Hungary,* no. 106-TUE-O1345-1158 in I06.

Dugda, M., Nyblade, A., Julia, J., Langston, C., Ammon, C. A. & Simiyu, S., 2005. Crustal structure in Ethiopia and Kenya from receiver function analysis: implications for rift development in eastern Africa, *J. geophys. Res.,* **110**(B01303), doi:10.1029/2004JB003065.

Dziak, R.P., Fox, C.G. & Schreiner, A.E., 1995. The June-July 1993 seismo-acoustic event at CoAxial segment, Juan de Fuca Ridge: evidence for a lateral dike injection, *Geophys. Res. Lett.,* **22**(2), 135–138.

Dziak, R.P., Smith, D.K., Bohnenstiehl, D.R., Fox, C.G., Desbruyeres, D., Matsumoto, H., Tolstoy, M. & Fornari, D.J., 2004. Evidence of a recent dike intrusion at the slow spreading Lucky Strike segment, Mid-Atlantic Ridge, *J. geophys. Res.,* **109**(B12102), doi:10.1029/2004JB003141.

Dziak, R.P., Bohnenstiehl, D.R., Cowen, J.P., Baker, E.T., Rubin, K.H., Haxel, J.H. & Fowler, M.J., 2007. Rapid dike emplacement leads to eruptions and hydrothermal plume release during sea-floor spreading events, *Geology,* **35,** doi:10.1130/G23476A.1.

Dziak, R.P., Bohnenstiehl, D.R., Matsumoto, H., Fowler, M.J., Haxel, J.H., Tolstoy, M. & Waldhauser, F., 2009. January 2006 seafloor-spreading event at 9°50'N, East Pacific Rise: ridge dike intrusion and transform fault interactions from regional hydroacoustic data, *Geochem. Geophys., Geosyst.,* 10:Q06T06, doi:10.1029/2009GC002388.

Ebinger, C.J., Ayele, A., Keir, D., Rowland, J., Yirgu, G., Wright, T., Belachew, M. & Hamling, I., 2010. Time and length scales of rift faulting and magma intrusion: the 2005-present Afar rifting cycle, *Ann. Rev. Earth Planet. Sci.,* **38,** 439–466.

Einarsson, P. & Brandsdóttir1980. Seismological evidence for lateral magma intrusion during the 1978 deflation of the Krafla volcano in NE-Iceland, *J. geophys. Res.,* **47,** 160–165.

Farr, T. & Kobrick, M., 2000. Shuttle radar topography mission produces a wealth of data, *EOS, Trans. Am. geophys. Un.,* **81,** 583–585.

Foulger, G.R., Kahn, C.H., Seeber, G., Einarsson, P., Julian, B.R. & Heki, K., 1992. Post-rifting stress relaxation at the divergent plate boundary in Northeast Iceland, *Nature,* **358,** 488–490.

Fukahata, Y. & Matsu'ura, M., 2005. General expressions for internal deformation fields dua to a dislocation source in a multilayered elastic half-space, *Geophys. J. Int.,* **161,** 507–521.

Fukahata, Y. & Matsu'ura, M., 2006. Quasi-static internal deformation due to a dislocation source in a multilayered elastic/viscoelastic half-space and an equivalence theorem, *Geophys. J. Int.,* **166,** 418–434.

Goldstein, R.M. & Werner, C.L., 1998. Radar interferogram filtering for geophysical applications, *Geophys. Res. Lett.,* **25**(21), 4035–4038.

Goldstein, R.M., Zebker, H.A. & Werner, C.L., 1988. Satellite radar interferometry: two-dimensional phase unwrapping, *Radio Sci.,* **23**(4), 713–720.

Grandin, R. *et al.*, 2009. September 2005 Manda Hararo-Dabbahu rifting event, Afar (Ethiopia): constraints provided by geodetic data, *Geophys. Res. Lett.,* **114,** doi:10.1029/2008JB005843.

Grandin, R., Socquet, A., Doin, M.P., Jacques, E., de Chabalier, J.-B. & King, G.C.P., 2010a. Transient rift opening in response to multiple dike injections in the Manda Hararo rift (Afar, Ethiopia) imagesd by time-dependent elastic inversion of interferometric synthetic aperture radar data, *J. geophys. Res.,* **115,** B09403, doi:10.1029/2009JB006883.

Grandin, R., Socquet, A., Jacques, E., Mazzoni, N., de Chabalier, J.-B. & King, G.C.P., 2010b. Sequence of rifting in Afar, Manda-Hararo rift, Ethiopia, 2005-2009: time-space evolution and interactions between dikes from interferometric synthetic aperture radar and static stress change modeling, *J. geophys. Res.,* **115,** B10413, doi:10.1029/2009JB000815.

Hamling, I.J. *et al.*, 2009. Geodetic observations of the ongoing Dabbahu rifting episode: new dyke intrusions in 2006 and 2007, *Geophys. J. Int.,* **172,** 989–1003.

Hamling, I.J., Wright, T.J., Calais, E., Bennati, L. & Lewi, E., 2010. Stress transfer between thirteen successive dyke intrusions in Ethiopia, *Nature Geosci.,* **3,** 713–717.

Hammond, J.O., Guidarelli, M., Belachew, M., Keir, D., Ayele, A., Ebinger, C., Stuart, G. & Kendall, J., 2008. Seismic observations from the Afar Rift Dynamics Project: preliminary results, *EOS, Trans. Am. geophys. Un.,* **89,** Fall meet. Suppl, T34A–1980.

Hammond, J.O.S., Kendall, J.M., Stuart, G.W. & Ebinger, C.J., 2009. Seismic imaging of the crust and upper mantle beneath Afar, Ethiopia, *EOS, Trans. Am. geophys. Un.,* **90,** Fall meet. Suppl, T31B–1808.

Hashima, A., Takada, Y., Fukahata, Y. & Matsu'ura, M., 2008. General expressions for internal deformation due to a moment tensor in an elastic/viscoelastic multilayered half-space, *Geophys. J. Int.,* **175,** 992–1012.

Hofton, M.A. & Foulger, G.R., 1996a. Postrifting anelastic deformation around the spreading plate boundary, north Iceland: 1. Modeling of the 1987-1992 deformation field using a viscoelastic Earth structure, *J. geophys. Res.,* **101**(B11), 25 403–25 421.

Hofton, M.A. & Foulger, G.R., 1996b. Postrifting anelastic deformation around the spreading plate boundary, north Iceland: 2. Implications of the model derived from the 1987–1992 deformation field, *J. geophys. Res.,* **101**(B11), 25 423–25 436.

Makris, J. & Ginzburg, A., 1987. The Afar depression: transition between continental rifting and sea-floor spreading, *Tectonophysics,* **141,** 199–214.

Massonnet, D. & Feigl, K.L., 1998. Radar Interferometry and its application to changes in the Earth's surface, *Rev. Geophys.,* **36,** 441–500.

Mogi, K., 1958. Relations between the eruptions of various volcanoes and the deformations of the ground surfaces around them, *Bull. Earthq. Res. Inst.,* **239,** 352–367.

Nooner, S.L., Bennati, L., Calais, E., Hamling, I.J., Wright, T.J., Buck, W.R. & Lewi, E., 2009. Post-rifting relaxation in the Afar region, Ethiopia, *Geophys. Res. Lett.,* **36**(L21308), doi:10.1029/2009GL040502.

Pagli, C., Wright, T.J., Ebinger, C.J., Barnie, T.D. & Ayele, A., 2009. Inflate, pause, erupt, recharge: the 1008 Alu eruption in the Erta'Ale volcanic system (Ethiopia), *EOS, Trans. Am. geophys. Un.,* **90**(54), Fall meet, Suppl, T31B–1813.

Pollitz, F.F. & Sacks, I.S., 1996. Viscosity structure beneath northeast Iceland, *J. geophys. Res.,* **101**(B8), 17771–17793.

Rosen, P.A., Hensley, S., Peltzer, G. & Simons, M., 2004. Updated repeat orbit interferometry package released, *EOS, Trans. Am. geophys. Un.,* **85**(5), 35.

Schmidt, D.A. & Burgmann, R., 2003. Time-dependent land uplift and subsidence in the Santa Clara valley, California, from a large interferometric, synthetic aperture radar dataset, *J. geophys. Res.,* **108,** 8534–8543.

Tiberi, C., Ebinger, C., Ballu, V., Stuart, G. & Oluma, B., 2005. Inverse models of gravity data from the Red Sea–Aden–East African Rift triple junction zone, *Geophys. J. Int.,* **163,** 775–787.

Tolstoy, M., Bohnenstiehl, D.R. & Edwards, M.H., 2001. Seismic character of volcanic activity at the ultraslow-spreading Gakkel Ridge, *Geology,* **29,** 1139–1142.

Tolstoy, M. *et al.*, 2006. A sea-floor spreading event captured by seismometers, *Science,* **314,** 1920–1922.

Tryggvason, E., 1984. Widening of the Krafla fissure swarm during the 1975-1981 Volcano-tectonic episode, *Bull. Volcanol,* **47**(1), 47–69.

Vigny, C., de Chablieer, J.-B., Ruegg, J.-C.P., Huchon, K.L.F., Cattin, R., Asfaw, L. & Kanbari, K., 2007. Twenty-five years of geodetic measurements along the Tadjoura-Asal rift system, Djibouti, East Africa, *J. geophys. Res.,* **112**(B06410), doi:10.1029/2004JB003230.

Wright, T.J., Ebinger, C., Biggs, J., Ayele, A., Yirgu, G., Keir, D. & Stork, A., 2006. Magma-maintained rift segmentation at continental rupture in the 2005 Afar dyking episode, *Nature,* **442,** 291–294.

Wright, T.J. *et al.*, 2012. Geophysical constraints on the dynamics of spreading centres from rifting episodes on land, *Nature Geosci.,* **5**(4), 242–250.